



# Hyperspectral time-domain terahertz nano-imaging

NEDA ALSADAT AGHAMIRI,<sup>1</sup> FLORIAN HUTH,<sup>2</sup> ANDREAS J. HUBER,<sup>2</sup>  
ALIREZA FALI,<sup>1</sup> RAINER HILLENBRAND,<sup>3,4</sup> AND YOHANNES ABATE<sup>1,\*</sup>

<sup>1</sup>*Department of Physics and Astronomy, University of Georgia, Athens, GA 30602, USA*

<sup>2</sup>*Neaspec GmbH, 82152 Martinsried, Germany*

<sup>3</sup>*CIC nanoGUNE and UPV/EHU, 20018 Donostia-San Sebastián, Spain*

<sup>4</sup>*IKERBARSQUE, Basque Foundation of Science, 48013 Bilbao, Spain*

\*yabate@physast.uga.edu

**Abstract:** Terahertz (THz) near-field microscopy has wide and unprecedented application potential for nanoscale materials and photonic-device characterization. Here, we introduce hyperspectral THz nano-imaging by combining scattering-type scanning near-field optical microscopy (s-SNOM) with THz time-domain spectroscopy (TDS). We describe the technical implementations that enabled this achievement and demonstrate its performance with a heterogeneously doped Si semiconductor sample. Specifically, we recorded a hyperspectral image of 40 by 20 pixels in 180 minutes and with a spatial resolution of about  $\sim$ 170 nm by measuring at each pixel with a time domain spectrum covering the range from 0.4 to 1.8 THz. Fitting the spectra with a Drude model allows for measuring—noninvasively and without the need for Ohmic contacts—the local mobile carrier concentration of the differently doped Si areas. We envision wide application potential for THz hyperspectral nano-imaging, including nanoscale carrier profiling of industrial semiconductor structures or characterizing complex and correlated electron matter, as well as low dimensional (1D or 2D) materials.

© 2019 Optical Society of America under the terms of the [OSA Open Access Publishing Agreement](#)

## 1. Introduction

Spectroscopy in the terahertz (THz) spectral range ( $\sim$ 0.1 THz to 10 THz) enables the investigation of low-energy (meV range) properties of matter such as molecular rotations, lattice vibrations, spin waves and internal excitations of bound electron–hole pairs and conductivities [1–3]. Due to the long wavelength of THz radiation, however, the spatial resolution of conventional THz spectroscopy is limited by diffraction to about 150  $\mu$ m (for a frequency of 1 THz, corresponding to a wavelength of 300  $\mu$ m).

The diffraction limit can be circumvented by scattering-type scanning near-field optical microscope (s-SNOM). s-SNOM is based on atomic force microscope (AFM), where a metal tip is illuminated with focused laser beam. The tip acts as an antenna and focuses the illumination to a nanoscale near-field spot at the tip apex. Near-field interaction between tip and sample modifies the tip scattered light. Interferometric detection of the tip scattered light thus allows for probing local refractive and absorption properties of the sample, by recording amplitude and phase of the scattered field, respectively. The resolution is essentially determined by the tip radius, which is in the range of about 25 nm for commercial metal coated tips [4].

Owing to its unique high-resolution imaging and spectroscopy capability, s-SNOM has been applied to interrogate a wide range of material properties in the THz frequency range. It has been used with monochromatic sources (gas lasers, free electron lasers, QCL), which allow for imaging and eventually spectroscopic imaging at selected wavelength [5–9]. s-SNOM has been also used with time domain spectroscopy (TDS) [10–13]. However, only point spectroscopy has been reported, i.e. spectra were acquired only at individual points. Imaging with TDS setups have been typically done with fixed delay line, where spectroscopy

information is lost. Altogether, either monochromatic imaging or point spectroscopy has been reported [5–13]. Hyperspectral imaging, that is a recording of 2D array of TDS near-field spectra has been not achieved yet.

Here, by combining s-SNOM with THz-TDS, we demonstrate hyperspectral THz nanoscopy in the frequency range spanning 0.5 THz to 1.8 THz, by imaging charge carrier profiles of a heterogeneously doped Si semiconductor sample. Hyperspectral imaging was achieved by increasing the detector signal (i) via forward detection of the tip-scattered THz field and (ii) by placing the whole microscope setup into a nitrogen purge box to reduce THz absorption by water in the beam paths. The forward detection allows for operation without the need for a beam splitter, which increases the tip-scattered THz field reaching the detector. It is enabled by a dual-beam parabolic mirror design. Hyperspectral images with a spatial resolution of about  $\sim 170$  nm were recorded by measuring at each pixel of a two-dimensional sample area a time domain spectrum covering 0.5 to 1.8 THz. By fitting individual THz TDS s-SNOM spectra with the help of the well-established finite dipole model of s-SNOM and a Drude model for doped Si, we measure the local mobile charge carrier density noninvasively and without the need of any Ohmic contacts.

## 2. Result and discussion

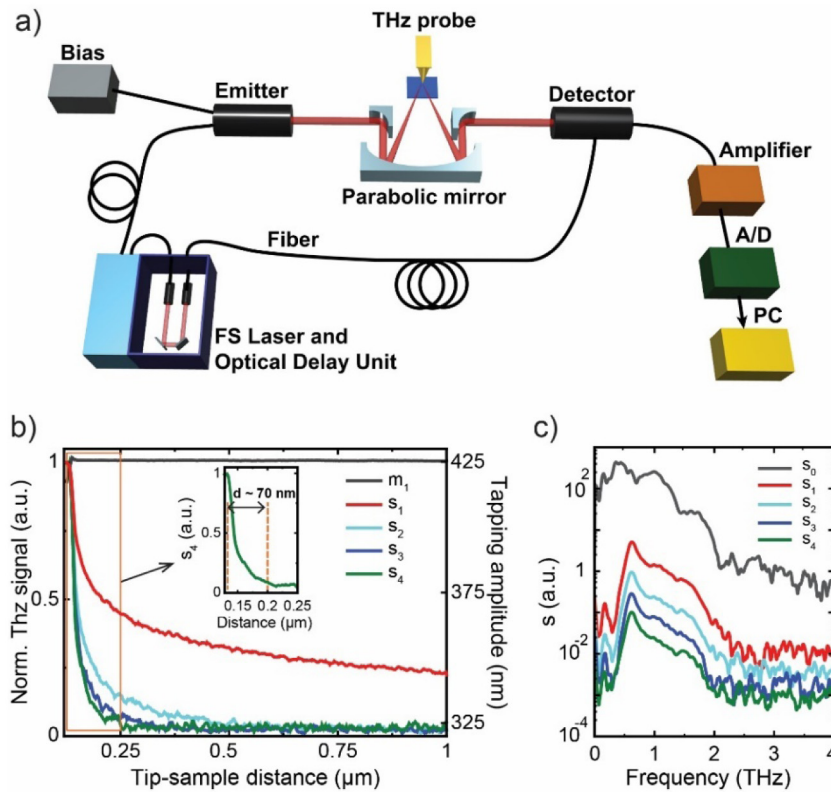


Fig. 1. Experimental setup and THz near field signal. (a) Schematic of THz-TDNS setup, (b) THz approach curve obtained with a commercial THz probe from Rocky mountain Tech taken on a Au surface, (c) far-field ( $S_0$ ) and near-field spectra  $s_n$  obtained by detector signal demodulation the  $n$ -th harmonic of the tip tapping frequency.

The THz time-domain nanospectroscopy (referred to as THz-TDNS) setup is shown in Fig. 1(a). It is a combination of a far-field broadband THz-TDS system (Menlo Co.) and a s-SNOM (Neaspec GmbH), see Appendix 1, Fig. 4(a) for picture. THz radiation is generated by pumping a photoconductive semiconductor InAs antenna using a femtosecond laser (Menlo

System) that has two fiber-coupled ports at  $\lambda = 1560$  nm and an average output power of 70 mW. One arm of the excitation femtosecond laser with a larger energy than the band gap of the semiconductor generates photo-induced free carriers that are accelerated by a bias field. The accelerated charges generate electromagnetic radiation at THz frequencies (see Fig. 1(c) for far-field power spectrum) [14]. This THz radiation is focused onto a commercial AFM tip (Rocky mountain model: 25PtIr200B-H) using the parabolic mirror of the s-SNOM. Instead of detecting the backscattered field, as typically done in s-SNOM, here the tip-scattered THz field is measured in the forward direction. This detection scheme is enabled by the dual-beam parabolic mirror design of the Neaspec s-SNOM (illustrated in Fig. 1(a)). It avoids the use of a beamsplitter (required in backscattering operation) and thus increases the tip-scattered THz field reaching the detector. A photoconductive antenna similar to the emitter is used in reverse for detecting the forward-scattered THz pulses without the need for a cooled detector. An optical delay line is used to measure the THz electric field as a function of time  $t$ , yielding  $E_{sca}(t)$ . Amplitude ( $s$ ) and phase ( $\phi$ ) spectra of the tip-scattered field are obtained by Fourier transform of  $E_{sca}(t)$ . All spectra were taken in a nitrogen atmosphere achieved by placing the THz-TDNS in a closed chamber filled with nitrogen (see Appendix 1, Fig. 4). Dry gas purging results in higher signal-to-noise ratio due to moisture removal.

The THz focus is diffraction limited (diameter  $\sim 150$   $\mu\text{m}$ ) and thus illuminates a large part of the tip shaft and sample region, which produces a strong background signal that overwhelms the near-field signal resulting from tip-sample near-field interaction. The background signal is removed by demodulating the detector signal at a higher harmonic  $n$  of the tip's oscillation frequency  $\Omega$ , as is routinely done in s-SNOM. The s-SNOM amplitude approach curves (Fig. 1(b)), acquired by measuring the demodulated detector signals as a function of the tip-sample distance at the  $n$ -th harmonic of the tip tapping frequency, illustrate the effect of signal demodulation. The  $s_n$  signals are maximum at small tip-sample distances and decrease rapidly as the tip is pulled away from the sample. With increasing demodulation order the signal decay more rapidly with distance, as well known from s-SNOM [12,15]. For this work, approach curves were recorded routinely before THz spectra or THz near-field images were taken, in order to assure that background artifacts are eliminated. Normalized amplitude ( $s_n(\text{sample}) / s_n(\text{reference})$ ) and phase ( $\phi_n(\text{sample}) - \phi_n(\text{reference})$ ) THz near-field spectra are obtained by taking first reference spectra on a reference area (such as gold or silicon), followed by taking spectra at a desired position of the sample surface. As probes we used commercial metal tips of a tip length of about  $L = 80$   $\mu\text{m}$  (Rocky mountain model: 25PtIr200B-H). In Fig. 5 (Appendix 1) we estimate the spatial resolution using line-profile analysis, yielding a value of about 170 nm. The topography and near-field amplitude line profiles were taken across regions C and D (Figs. 5(a)–(d)). The spatial resolution was calculated by taking the full width at half maximum (FWHM) of the line spread function (Fig. 5(e)), which is found by taking the derivative of the amplitude line profile [16,17].

THz nano-spectroscopy enables noninvasive and contactless nanoscale carrier profiling of doped structures. To demonstrate this capability of our THz-TDNS setup, we studied a pre-characterized silicon static random access memory (SRAM) sample. The topography image (Fig. 2(a)) shows several features between about 40 and 420 nm in height, which relate to implanted regions. According to the SRAM manufacturer, region D is the homogeneously *p*-doped substrate with a nominal hole density,  $n_p = 2 \times 10^{16} \text{ cm}^{-3}$ . Regions A, B and C are ion implanted. A is *p*-type with hole density,  $n_p = 4 \times 10^{19} \text{ cm}^{-3}$ , B and C are *n*-type with electron densities,  $n_e = 1 \times 10^{17} \text{ cm}^{-3}$  and  $n_e = 2 \times 10^{17} \text{ cm}^{-3}$ , respectively. The near-field amplitude image  $s_2$  shown in Fig. 2(b) was taken by focusing the broadband THz radiation onto the tip and raster scanning the sample. At a fixed reference mirror position the scattered field from the tip-sample interface was collected. The detector signal was demodulated at the second harmonic of the tip's mechanical resonance frequency, yielding the background-free broadband  $s_2$ -image shown in Fig. 2(b). It reveals the presence of regions with varying dopant levels.

For spectroscopic characterization of the different doping regions, the tip was illuminated again with the THz radiation generated by pumping a photoconductive semiconductor InAs antenna as described above. A delay stage varies the arrival time of the optical gate pulse on the detector with respect to the tip-scattered THz pulse. Scanning the delay line allows for recording the electric field of the tip-scattered THz radiation as a function of time. Subsequent Fourier transform of the demodulated detector signal (demodulation order  $n = 2$ ) yields background-free THz near-field amplitude and phase spectra. To obtain normalized nano-THz spectra, we took broadband spectra at different points on the sample (shown A-D in Figs. 2(a) and 2(b)) and normalized them to a reference point shown as Ref. This reference point has a nominal electron density of  $2 \times 10^{20} \text{ cm}^{-3}$ , which implies that this region is metallic in the 0.4 to 1.8 THz spectral range. It thus can be used as a suitable reference to normalize the near-field spectra obtained on the regions A-D, analogously to normalizing to a Au or Si silicon surface as routinely done in nano-FTIR spectroscopy [12,18,19]. The experimental amplitude and phase point spectra are shown in Figs. 2(c) and 2(e), respectively. We find that the average amplitude signal is different on the different sample regions, and generally tends to decrease with increasing frequency (Fig. 2(c)). The phase spectra displayed in Fig. 2(e) show also show noticeably different spectra at the various doping regions. Particularly, the phase spectrum taken at point D shows decreasing phase with increasing frequency, while the spectra at points A-C exhibit an increasing phase with increasing frequency.

In order to analyze and interpret the THz TDNS spectra we performed model calculations using the well-established finite dipole model assuming a Drude-type dielectric function for the doped sample regions [20–22]. The model describes the tip by a metallic ellipsoid with a length of 600 nm and 40 nm apex radius, being illuminated at an angle of 60° relative to the tip axis. The tip-scattered field is given by  $E_s = s \exp(i\phi) \propto (1 + r_p)^2 \alpha_{\text{eff}} E_{\text{inc}}$ , where  $r_p$  is the far-field Fresnel reflection coefficient of the sample [22],  $E_{\text{inc}}$  the incident electric field and  $\alpha_{\text{eff}}$  the effective polarizability of the tip [23] that is governed by the near-field interaction between tip and sample (see Appendix 2). The local sample properties, i.e. the electron and hole densities  $n_e$  and  $n_p$ , are included in  $r_p$  via the dielectric function of the sample. The presence of free carrier result in a Drude term given by the dielectric function  $\epsilon(n, \omega) = \epsilon_\infty (1 - (\omega_p^2 / (\omega^2 + i\omega\gamma)))$  where  $\epsilon_\infty = 11.9$ ,  $\omega_p = \sqrt{n e^2 / m^* \epsilon_0}$  is plasma frequency ( $m^*$  is the effective mass of electron and  $n$  is carrier concentration ( $n_p$  or  $n_e$ ) and  $\gamma$  is the damping constant, and is inversely proportional to the carrier concentration-dependent mobility  $\mu(n)$  as  $\gamma \sim 1/\mu(n_{p,e})$  [24] (for more details on the parameters and equations used see Appendix 2). Our calculations include tip-sample distance modulation and higher-harmonic signal demodulation, yielding amplitude and phase spectra,  $s_n(\omega)$  and  $\varphi_n(\omega)$  respectively [22]. Figures 2(d) and 2(f) show the calculated near-field amplitude  $s_2$  and phase  $\varphi_2$  spectra for the regions A-D, normalized to the  $n$ -doped Si region marked as Ref in Fig. 2(a). The carrier densities  $n_e$  and  $n_p$  were chosen such that best agreement with the experimental spectra (Figs. 2(c) and 2(e)) was achieved. They are shown in Table 1 and compared with the nominal values we find reasonable agreement. Quantitative differences we explain by uncertainties in the model, which does not account for the realistic tip geometry (tip length and apex radius).

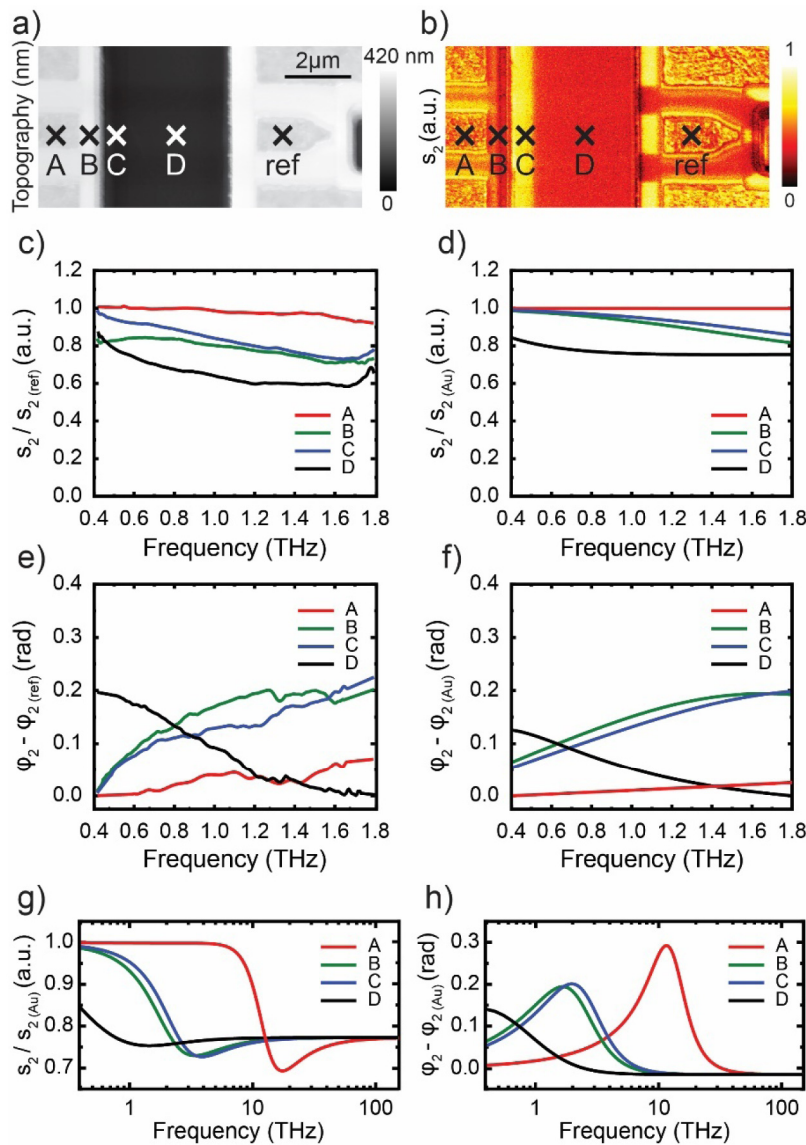


Fig. 2. THz TDS nanospectroscopy and broadband nanoimaging. (a) Topography image of SRAM sample described in main text, (b) broadband THz near-field amplitude image  $s_2$ , revealing different doping regions; D is the homogeneously p-doped substrate with nominal hole density of  $2 \times 10^{16} \text{ cm}^{-3}$ ; A, B & C are ion implanted with values: A p-type with hole density  $4 \times 10^{19} \text{ cm}^{-3}$ , B and C n-type with electron densities of  $1 \times 10^{17} \text{ cm}^{-3}$  and  $2 \times 10^{17} \text{ cm}^{-3}$ , respectively, (c) THz-TDNS amplitude  $s_2$  and (e) phase  $\varphi_2$  spectra at points A, B, C and D, (d) & (f) calculated THz amplitude  $s_2$  and phase  $\varphi_2$  spectra of near-field contrast in 0.4–1.8 THz, (g) & (h) calculated THz amplitude  $s_2$  and phase  $\varphi_2$  spectra of near-field contrast in an extended spectral range. Finite dipole model was used for the calculation resulting in p-doped Si fitted values  $1 \times 10^{19}$ ,  $3 \times 10^{17}$ ,  $4 \times 10^{17}$ , and  $4 \times 10^{16} \text{ cm}^{-3}$  for A, B, C and D, respectively, see Table 1.

The spectra and their variation with carrier concentration can be understood as follows. The tip-sample near-field interaction for a Drude-type semiconductor sample results in a step (respectively a weak resonance peak) in the amplitude spectrum near the plasma frequency  $\omega_p$  [9,25,26], which is accompanied by a peak in the phase spectrum (Figs. 2(g) and 2(h)).

The spectral behavior can be explained by a tip-induced plasmon resonance in the sample. Since the plasma frequency increases with carrier density, the amplitude step and phase peak shift to higher frequencies for higher carrier concentrations. This explains why the areas of higher carrier concentration (A, B, C) exhibit their phase maxima at frequencies larger than 1.8 THz, while area D (lowest doping concentration) shows a phase maximum at frequencies lower than 0.4 THz.

**Table 1. SRAM specification and fitted values for doping concentrations**

	Type	Nominal concentration (cm <sup>-3</sup> )	Fitted concentration using finite dipole model
Reference	n <sup>+</sup>	$2 \times 10^{20}$	
A	p <sup>+</sup>	$4 \times 10^{19}$	$1 \times 10^{19}$
B	n <sup>-</sup>	$1 \times 10^{17}$	$3 \times 10^{17}$
C	n-well	$2 \times 10^{17}$	$4 \times 10^{17}$
D	p-epi	$2 \times 10^{16}$	$4 \times 10^{16}$

In Fig. 3 we demonstrate the capability of the THz-TDNS setup for hyperspectral nanoimaging. To that end, we measured an array of 40 by 20 tip-enhanced TDS spectra at the *n-p* transition region between regions C and D marked in Fig. 3(b) of the SRAM sample. The acquisition time for each spectrum was 13.5 seconds, thus yielding a total acquisition time of 3 hours. After normalization of each spectrum to a reference spectrum, a hyperspectral amplitude (Fig. 3(c)) and phase (Fig. 3(d)) data cube  $A(x,y,\omega)$  was obtained, with *x* and *y* indicating the plane of the sample surface and the *z*-axis corresponding to the frequency axis (0.5 to 1.8 THz). All spectra are taken in a closed chamber filled with nitrogen (Appendix 1, Fig. 4). Clearly, the hyperspectral data reproduce the spectral features on the regions C and D, as discussed above (Fig. 2). Most important, the quality of the hyperspectral data (i.e. the signal-to-noise ratio and signal stability) allows for extracting monochromatic amplitude and phase images in the broad range between 0.6 and 1.6 THz, where imaging up to now has been only possible at limited frequencies from gas or quantum cascade lasers [5–10,13]. We observe homogenous signal levels on both sides of the p-n junction. At the junction itself we observe a signal transition of a few 100 nm width, which can be attributed to carrier diffusion [7] and the spatial resolution of about 170 nm (Appendix 1, Fig. 5). In the future, THz hyperspectral data cubes could offer more sophisticated analysis possibilities as compared to individual images and spectra. For example, 2D carrier maps could be extracted by fitting the individual spectra, or multivariate data analysis could be applied (analogous to hyperspectral IR nanoimaging). We abstain from such analysis of the data cube presented in Fig. 3 because of the complexity of the p-n junction. Note that the individual spectra cannot be fitted with the use of a simple Drude term like inside the homogeneous regions C and D, as carrier diffusion leads, for example, to the local presence of both hole and electrons exhibiting different effective masses. A detailed analysis of the carrier local carrier concentration would thus go too far beyond the scope of this paper, which is the technical description and demonstration of THz hyperspectral nanoimaging.

We finally note that near-field images taken at mid infrared (28 THz) or visible (474 THz) frequencies [see Appendix 1, Fig. 6] do not show contrast between the differently doped regions. This observation is consistent with the calculations shown in Figs. 2(g) and 2(h) and highlights the importance of near-field imaging and spectroscopy at THz frequencies.

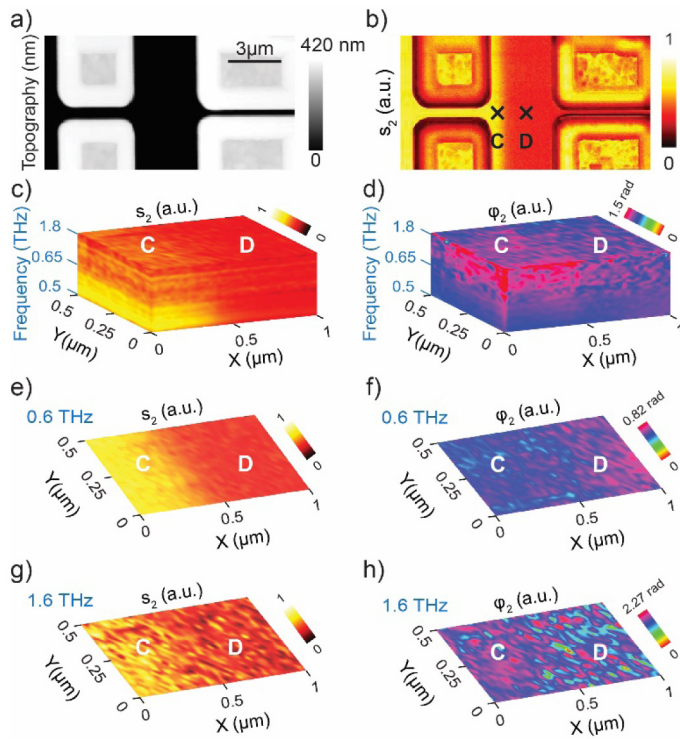


Fig. 3. Hyperspectral Nano-Imaging. (a) Topography, (b) second harmonic broadband THz near-field amplitude  $s_2$  images of SRAM sample, regions C and D are indicated, (c) 3D hyperspectral THz Amplitude  $s_2$  and (d) Phase  $\phi_2$  data cube at transition regions covering C and D with different doping level in the range of 0.5-1.8 THz, (e) second harmonic amplitude  $s_2$  and (f) phase  $\phi_2$  at transition regions covering C and D at 0.6 THz extracted from part c, (g) and (h) second harmonic amplitude  $s_2$  and (f) phase  $\phi_2$  at transition regions covering C and D at 1.6 THz extracted from part d.

### 3. Conclusion

In summary, we introduced THz-TDNS (which combines s-SNOM with THz-TDS) for THz hyperspectral nano-imaging. We described the technical details and demonstrated the acquisition of hyperspectral data cubes of a semiconductor p-n junction. Data cubes consisting of 40 by 20 spectra were obtained in 3 hours. The THz-TDNS is designed to fit on kinematic mounts on either side of the AFM tip and is easily removal allowing for s-SNOM or tip-enhanced Raman or photoluminescence operation on the same neaSNOM platform. In addition, the THz-TDNS compact design avoids the need for a beam splitter (enabling increased detected signal) and cooled detectors. We anticipate wide application potential for THz hyperspectral nanoimaging, including fast and non-invasive spectroscopic quantitative sampling of carrier densities in semiconductor nano-structures, complex and correlated oxides, low dimensional (1D or 2D) materials' interfaces and boundaries at high spatial resolutions.

## Appendix 1

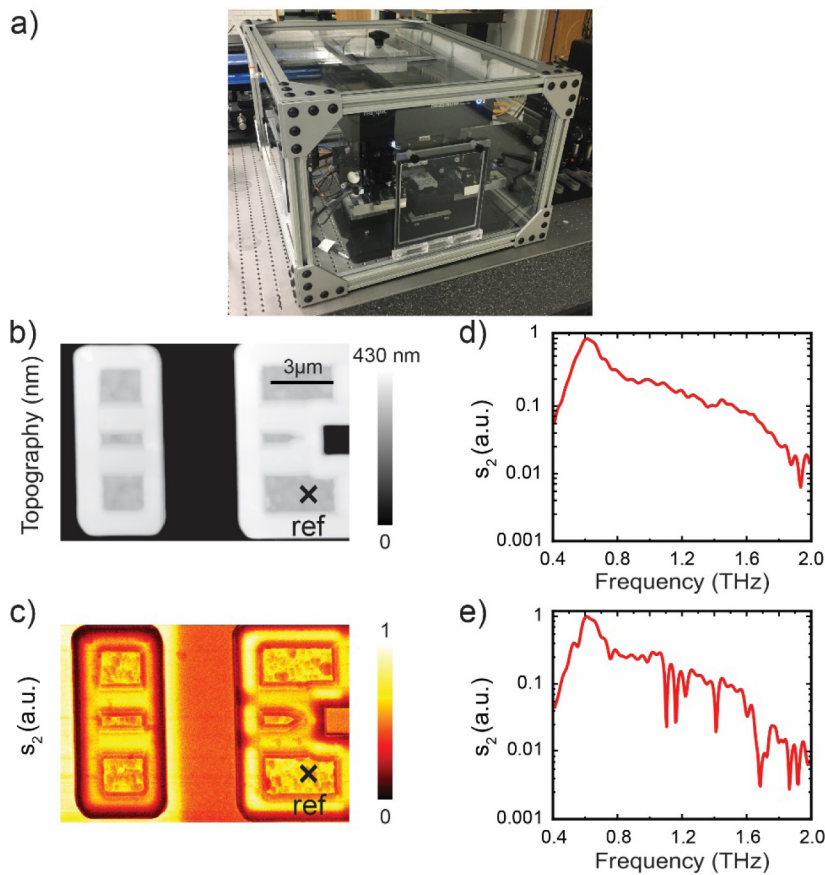


Fig. 4. (a) Picture of THz-TDNS setup in a nitrogen purge box, (b) topography and (c) second harmonic broadband near field amplitude  $s_2$  image of SRAM sample, (d) THz TDNS amplitude  $s_2$  spectra measured at marked position of reference marked in (b) & (c) in dry nitrogen environment and (e) in ambient.

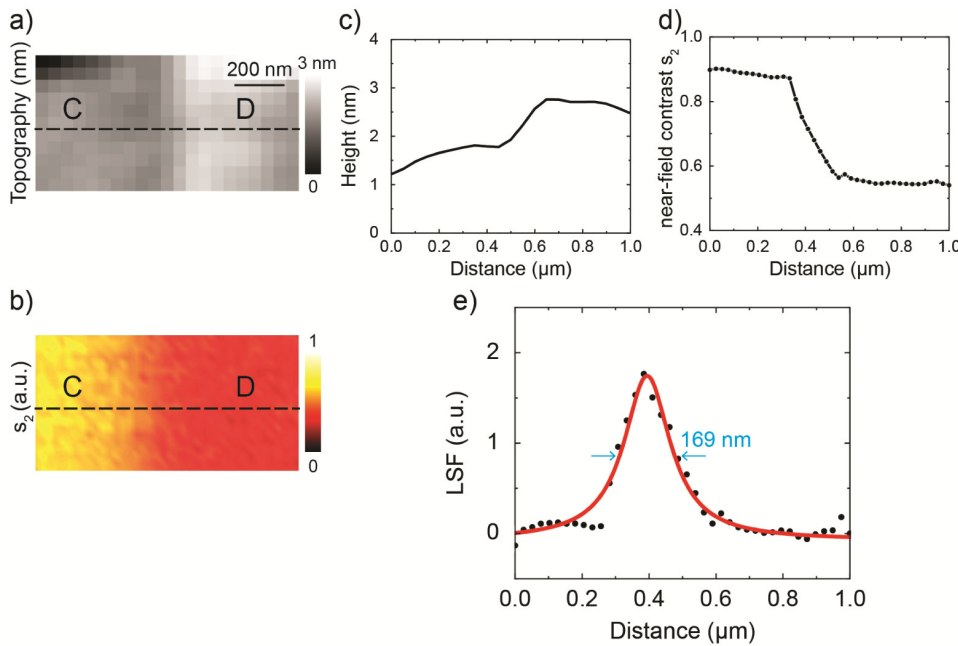


Fig. 5. (a) Topography and (b) second harmonic monochromatic near field amplitude  $s_2$  image extended from region C to region D taken at 0.6 THz (extracted from hyperspectral image), (c) topography line profile extended along dash line in (a), (d) amplitude  $s_2$  line profile extended along averages of several dash lines in (b), (e) derivate of lines profile of part (d) (dots) with symmetric Lorentzian fit (red line) and FWHM (blue arrows).

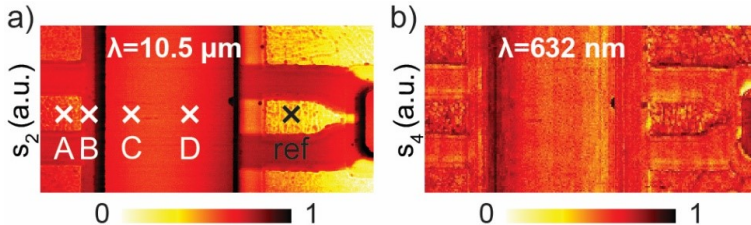


Fig. 6. (a) Second harmonic near field amplitude  $s_2$  image taken at mid IR wavelength,  $\lambda = 10.5 \mu\text{m}$  (28 THz), (b) forth harmonic near field amplitude  $s_4$  image taken at visible wavelength,  $\lambda = 632 \text{ nm}$  (474 THz).

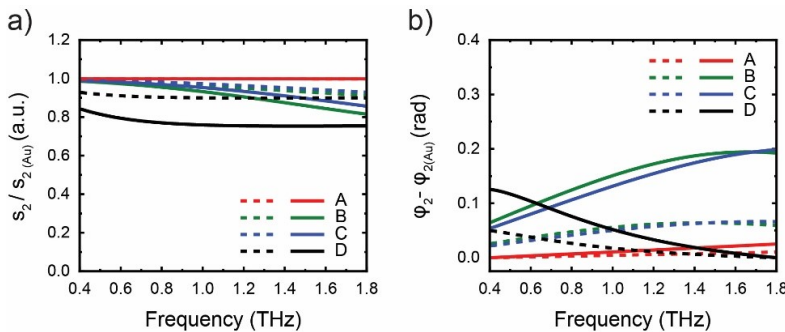


Fig. 7. (a) Simulated THz amplitude  $s_2$  and (b) phase  $\varphi_2$  spectra of near-field contrast for regions A,B, C and D. Finite dipole model was used for the calculation resulting in  $p$ -doped Si fitted values  $1 \times 10^{19}$ ,  $3 \times 10^{17}$ ,  $4 \times 10^{17}$ , and  $4 \times 10^{16} \text{ cm}^{-3}$  for A, B, C and D respectively, dash lines are simulated spectra without considering of reflection coefficient ( $r_p = 0$ ).

## Appendix 2

### 2.1. Fresnel reflection coefficient $r_p$ and effective polarizability $\alpha_{\text{eff}}$

Equations (1) and (2) are used to calculate Fresnel coefficient ( $r_p$ ) for  $p$ -doped silicon with thickness of  $d_1$  [22]. Note that if  $r_p$  is not taken into account in the calculation, simulated results do not give the best fit to experimental data (see Appendix 1, Fig. 7 for comparison simulation with and without  $r_p$ ). In these equations  $\epsilon_1$  is dielectric function of doped silicon,  $\epsilon_2$  is dielectric constant of the substrate which we assume  $\epsilon_2 = \epsilon_{si} = 11.9$ ,  $\epsilon_0 = 8.85 \times 10^{-12}$  Fm<sup>-1</sup> and  $R_t$  is tip curvature radius which is 40 nm.

$$r_p(q, \omega) \approx \frac{\epsilon_* - \epsilon_0}{\epsilon_* + \epsilon_0} \quad (1)$$

$$\epsilon_* \approx \epsilon_1 \frac{\epsilon_2 + \epsilon_1 \tan h(qd_1)}{\epsilon_1 + \epsilon_2 \tan h(qd_1)}; q \sim \frac{1}{R_t} \quad (2)$$

Eqs. (3)–(9) give us the effective polarizability [23].  $L$  is effective length of tip which considered 600 nm,  $R_t$  is tip curvature radius,  $C$  is the height-independent constant with  $Q_0 = R_t^2 E_0$  which is the total amount of the polarization charge induced in tip in the absence of sample which is described in [21],  $H$  is tip and sample distance.

$$\alpha_{\text{eff}} = C \left( 1 + \frac{f_0(H)\beta(\epsilon)}{2(1-f(H)\beta(\epsilon))} \right) \quad (3)$$

$$f_0(H) = \left( g - \frac{2H + W_0 + R_t}{2L} \right) \frac{\ln\left(\frac{4L}{4H + 2W_0 + R_t}\right)}{\ln\left(\frac{4L}{R_t}\right)} \quad (4)$$

$$f(H) = \left( g - \frac{2H + W_i + R_t}{2L} \right) \frac{\ln\left(\frac{4L}{4H + 2R_t}\right)}{\ln\left(\frac{4L}{R_t}\right)} \quad (5)$$

$$C = \frac{LQ_0}{|E_0|} \quad (6)$$

$$\beta = \frac{\epsilon_{\text{doped(si)}} - 1}{\epsilon_{\text{doped(si)}} + 1} \quad (7)$$

$$W_0 \approx \frac{1.31R_t L}{(L + 2R_t)} \quad (8)$$

$$W_i \approx \frac{R_t}{2} \quad (9)$$

## 2.2. Dielectric function of *p*-doped Si

Equations (10)–(12) are used to calculate the dielectric function in presence of carrier mobilities [26]. Here  $\epsilon_{\infty} = 11.9$  is the high-frequency dielectric constant of Si,  $\omega_p$  is plasma frequency and  $\gamma$  is damping. (In calculation we used the dielectric function of *p*-doped Si for all four regions of A, B, C and D since the difference in dielectric function of *p*-doped and *n*-doped Si is very small and we assume that they are relatively the same.)

$$\epsilon_{doped(si)}(\omega_{nd}) = \epsilon_{\infty}(1 - \frac{\omega_p^2}{\omega^2 + i\omega\gamma}) \quad (10)$$

$$\omega_p = ((\frac{nd \times e^2 \times 10^6}{\epsilon_0 \epsilon_{\infty} m^*})^{1/2} \times \frac{1}{200\pi c_0}) \quad (11)$$

$$\gamma = \frac{100e}{2\pi c_0 m^* ((\mu_0 \exp(-pc/nd)) + (\frac{\mu_{max}}{1 + (\frac{nd}{Cr})^\alpha}) - (\frac{\mu_1}{1 + (\frac{Cs}{nd})^\beta}))} \quad (12)$$

Constant in the equations above are:  $\epsilon_{\infty} = 11.9$ ,  $\epsilon_0 = 8.85 \times 10^{-12}$ ,  $e = 1.60218 \times 10^{-19}$ ,  $m_{electron}^* = 0.26m_0$ ,  $m_{hole}^* = 0.37m_0$ ,  $m_0 = 0.91095 \times 10^{-30}$ ,  $c_0 = 2.99792 \times 10^8$ ,  $\mu_0 = 44.9$ ,  $\mu_1 = 7$ ,  $\mu_{max} = 470.5$ ,  $pc = 9.26 \times 10^{16}$ ,  $Cr = 2.33 \times 10^{17}$ ,  $Cs = 6.1 \times 10^{20}$ ,  $\alpha = 0.779$ ,  $\beta = 2$ .

## Funding

U.S. Army Research Office/Air Force Office of Scientific Research (ARO/AFOSR) (W911NF-16-1-0495); Air Force Office of Scientific Research (AFOSR) (FA9559-16-1-0172); National Science Foundation (1553251); Spanish Ministry of Science, Innovation and Universities (RTI2018-094830-B-I00).

## Acknowledgments

YA and NA gratefully acknowledge support provided by the Air Force Office of Scientific Research (AFOSR) grant number FA9559-16-1-0172. The work of AF is supported by the National Science Foundation grant no. 1553251. RH acknowledges funding from the Spanish Ministry of Science, Innovation and Universities (project RTI2018-094830-B-I00). The authors acknowledge useful discussions with Fritz Keilmann (Ludwig-Maximilians-Universität). YA acknowledges Kenneth C. Goretta (AFOSR) for assistance during the initial acquisition of funds for this work.

## References

1. T. Kampfrath, K. Tanaka, and K. A. Nelson, “Resonant and nonresonant control over matter and light by intense terahertz transients,” *Nat. Photonics* **7**(9), 680–690 (2013).
2. S. S. Dhillon, M. S. Vitiello, E. H. Linfield, A. G. Davies, M. C. Hoffmann, J. Booske, C. Paoloni, M. Gensch, P. Weightman, G. P. Williams, E. Castro-Camus, D. R. S. Cumming, F. Simoens, I. Escorcia-Carranza, J. Grant, S. Lucyszyn, M. Kuwata-Gonokami, K. Konishi, M. Koch, C. A. Schmuttenmaer, T. L. Cocker, R. Huber, A. G. Markelz, Z. D. Taylor, V. P. Wallace, J. Axel Zeitzer, J. Sibik, T. M. Korter, B. Ellison, S. Rea, P. Goldsmith, K. B. Cooper, R. Appleby, D. Pardo, P. G. Huggard, V. Krozer, H. Shams, M. Fice, C. Renaud, A. Seeds, A. Stöhr, M. Naftaly, N. Ridler, R. Clarke, J. E. Cunningham, and M. B. Johnston, “The 2017 terahertz science and technology roadmap,” *J. Phys. D Appl. Phys.* **50**(4), 043001–043049 (2017).
3. J. Lloyd-Hughes and T. I. Jeon, “A Review of the Terahertz Conductivity of Bulk and Nano-Materials,” *J. Infrared Millim. Terahertz Waves* **33**(9), 871–925 (2012).
4. F. Keilmann, A. J. Huber, and R. Hillenbrand, “Nanoscale Conductivity Contrast by Scattering-Type Near-Field Optical Microscopy in the Visible, Infrared and THz Domains,” *J. Infrared Millim. Terahertz Waves* **30**, 1255–1268 (2009).

5. M. C. Giordano, S. Mastel, C. Liewald, L. L. Columbo, M. Brambilla, L. Viti, A. Politano, K. Zhang, L. Li, A. G. Davies, E. H. Linfield, R. Hillenbrand, F. Keilmann, G. Scamarcio, and M. S. Vitiello, "Phase-resolved terahertz self-detection near-field microscopy," *Opt. Express* **26**(14), 18423–18435 (2018).
6. F. Kuscheswski, H.-G. Ribbeck, J. Döring, S. Winnerl, L. M. Eng, and S. C. Kehr, "Narrow-band near-field nanoscopy in the spectral range from 1.3 to 8.5 THz," *Appl. Phys. Lett.* **108**(11), 113102 (2016).
7. C. Liewald, S. Mastel, J. Hesler, A. J. Huber, R. Hillenbrand, and F. Keilmann, "All-electronic terahertz nanoscopy," *Optica* **5**(2), 159–163 (2018).
8. H. T. Chen, R. Kersting, and G. C. Cho, "Terahertz imaging with nanometer resolution," *Appl. Phys. Lett.* **83**(15), 3009–3011 (2003).
9. A. J. Huber, F. Keilmann, J. Wittborn, J. Aizpurua, and R. Hillenbrand, "Terahertz Near-Field Nanoscopy of Mobile Carriers in Single Semiconductor Nanodevices," *Nano Lett.* **8**(11), 3766–3770 (2008).
10. K. Moon, H. Park, J. Kim, Y. Do, S. Lee, G. Lee, H. Kang, and H. Han, "Subsurface Nanoimaging by Broadband Terahertz Pulse Near-Field Microscopy," *Nano Lett.* **15**(1), 549–552 (2015).
11. H. T. Stinson, A. Sternbach, O. Najera, R. Jing, A. S. Mcleod, T. V. Slusar, A. Mueller, L. Anderegg, H. T. Kim, M. Rozenberg, and D. N. Basov, "Imaging the nanoscale phase separation in vanadium dioxide thin films at terahertz frequencies," *Nat. Commun.* **9**(1), 3604 (2018).
12. H. G. von Ribbeck, M. Brehm, D. W. van der Weide, S. Winnerl, O. Drachenko, M. Helm, and F. Keilmann, "Spectroscopic THz near-field microscope," *Opt. Express* **16**(5), 3430–3438 (2008).
13. J. Zhang, X. Chen, S. Mills, T. Ciavatti, Z. Yao, R. Mescall, H. Hu, V. Semenenko, Z. Fei, H. Li, V. Perebeinos, H. Tao, Q. Dai, X. Du, and M. Liu, "Terahertz Nanoimaging of Graphene," *ACS Photonics* **5**(7), 2645–2651 (2018).
14. R. M. Smith and M. A. Arnold, "Terahertz Time-Domain Spectroscopy of Solid Samples: Principles, Applications, and Challenges," *Appl. Spectrosc. Rev.* **46**(8), 636–679 (2011).
15. N. Ocelic, A. Huber, and R. Hillenbrand, "Pseudoheterodyne detection for background-free near-field spectroscopy," *Appl. Phys. Lett.* **89**(10), 101124 (2006).
16. C. Maissen, S. Chen, E. Nikulina, A. Govyadinov, and R. Hillenbrand, "Probes for Ultrasensitive THz Nanoscopy," *ACS Photonics* **6**(5), 1279–1288 (2019).
17. S. Mastel, A. A. Govyadinov, C. Maissen, A. Chuvalin, A. Berger, and R. Hillenbrand, "Understanding the Image Contrast of Material Boundaries in IR Nanoscopy Reaching 5 nm Spatial Resolution," *ACS Photonics* **5**(8), 3372–3378 (2018).
18. F. Huth, A. Govyadinov, S. Amarie, W. Nuansing, F. Keilmann, and R. Hillenbrand, "Nano-FTIR Absorption Spectroscopy of Molecular Fingerprints at 20 nm Spatial Resolution," *Nano Lett.* **12**(8), 3973–3978 (2012).
19. S. Amarie, T. Ganz, and F. Keilmann, "Mid-infrared near-field spectroscopy," *Opt. Express* **17**(24), 21794–21801 (2009).
20. F. Keilmann and R. Hillenbrand, *Near-Field Nanoscopy by Elastic Light Scattering from a Tip* (Artech House, 2009).
21. A. Cvitkovic, N. Ocelic, and R. Hillenbrand, "Analytical model for quantitative prediction of material contrasts in scattering-type near-field optical microscopy," *Opt. Express* **15**(14), 8550–8565 (2007).
22. L. M. Zhang, G. O. Andreev, Z. Fei, A. S. McLeod, G. Dominguez, M. Thiemens, A. H. Castro-Neto, D. N. Basov, and M. M. Fogler, "Near-field spectroscopy of silicon dioxide thin films," *Phys. Rev. B Condens. Matter Mater. Phys.* **85**(7), 075419 (2012).
23. A. A. Govyadinov, I. Amenabar, F. Huth, P. S. Carney, and R. Hillenbrand, "Quantitative Measurement of Local Infrared Absorption and Dielectric Function with Tip-Enhanced Near-Field Microscopy," *J. Phys. Chem. Lett.* **4**(9), 1526–1531 (2013).
24. J. M. Stiegler, A. J. Huber, S. L. Diedenhofen, J. G. Rivas, R. E. Algra, E. P. Bakkers, and R. Hillenbrand, "Nanoscale Free-Carrier Profiling of Individual Semiconductor Nanowires by Infrared Near-Field Nanoscopy," *Nano Lett.* **10**(4), 1387–1392 (2010).
25. B. Knoll and F. Keilmann, "Infrared conductivity mapping for nanoelectronics," *Appl. Phys. Lett.* **77**(24), 3980–3982 (2000).
26. A. J. Huber, D. Kazantsev, F. Keilmann, J. Wittborn, and R. Hillenbrand, "Simultaneous IR Material Recognition and Conductivity Mapping by Nanoscale Near-Field Microscopy," *Adv. Mater.* **19**(17), 2209–2212 (2007).